Nuclear Instruments and Methods in Physics Research A 596 (2008) 317–326

Contents lists available at ScienceDirect

Nuclear Instruments and Methods in Physics Research A

journal homepage: www.elsevier.com/locate/nima

The in-flight performance of the X-ray Solar Monitor (XSM) on-board SMART-1

L. Alha [a,*], J. Huovelin [a], T. Hackman [a], H. Andersson [b], C.J. Howe [c], Eero Esko [a], M. Väänänen [a]

[a] Observatory, University of Helsinki, P.O. Box 14, FI-00014 Helsinki, Finland
[b] Oxford Instruments Analytical, P.O. Box 85, FI-02631 Espoo, Finland
[c] Rutherford Appleton Laboratory, Chilton, Didcot OX11 0QX, UK

ARTICLE INFO

Article history:
Received 3 July 2008
Accepted 17 August 2008
Available online 5 September 2008

Keywords:
X-ray detectors
Solar X-rays
Spectral response
Effective area

ABSTRACT

The operation, performance, and in-flight calibrations of the X-ray Solar Monitor (XSM) on-board ESA's SMART-1 mission to the Moon are presented. The basic method of deriving the response and effective area of the XSM is described. The evolution of the energy resolution as a function of time is studied, and sample data of high quality broadband solar flare spectra including highly ionized Fe-lines are also presented.

1. XSM scientific objectives

XSM (X-ray Solar Monitor) was an X-ray spectrometer on-board the SMART-1 [1] mission to the Moon. The launch of SMART-1 was on 27th of September 2003 [2], and regular operations of payload instruments were initialized during the period February–March 2004. The mission lifetime was extended, and ended with the scheduled impact on the Moon on September 3, 2006. The results of SMART-1 science are described in Ref. [3]. The main task of XSM was to monitor the solar coronal X-ray spectrum in the nominal energy range 2–20 keV with sufficient energy resolution for estimates of the X-ray fluorescence of the lunar surface.

1.1. Lunar science

The main science goal of the D-CIXS (Demonstration of a Compact Imaging X-ray Spectrometer, [4]) on SMART-1 was to produce the first global map of the Moon in X-rays. D-CIXS made position sensitive measurements of the X-ray spectrum emitted by the surface of the Moon, which includes fluorescence lines by chemical elements of the lunar surface. XSM was the solar calibration instrument. XSM monitored the variable solar X-ray output simultaneously with D-CIXS measurements. The primary solar X-ray output must be known to properly understand the fluorescent spectra emitted by the Moon. The chemical composition of the lunar surface can, in principle, be determined by applying a detailed analysis of the X-ray spectroscopy by the two instruments, i.e. measurements of the Moon and the Sun. However, the X-ray emission of the Moon is weak, and the lower energy part of the studied spectral range (~1–10 keV) is very densely populated with emission lines. It is difficult to resolve contributions by individual chemical elements and the results are thus limited to only a few chemical elements.

1.2. Solar science

In addition to being necessary for the Moon science, the data of XSM [5] are also used for solar science. Proper analysis of XSM spectra for solar science does not require data from D-CIXS. During the cruise phase of the mission, XSM observed the solar X-ray output for 439 h in total. The data obtained during this period include several tens of solar flares, as well as quiescent periods. Since the data are of high time resolution (16 s per spectrum), it enables a detailed study of the rise and decay of virtually all detected flare events down to a flux level at 0.1–0.8 nm of $\sim 10^{-7}$ W/m^2, i.e. corresponding to B1 level flares. XSM was also sensitive enough to see the 2–10 keV quiescent Sun spectrum at solar minimum ($\sim 10^{-8}$ W/m^2 at 0.1–0.8 nm), and even the X-ray sky spectrum, since the instrument background and noise of the detector was very low. In principle any number of adjacent spectra could be summed up to improve the S/N ratio, if the source flux remained constant, and environmental conditions (S/C temperature and space particle radiation) were favorable for the operation

* Corresponding author. Tel.: +358 9 19121772; fax: +358 9 19122952.
E-mail address: alha@mappi.helsinki.fi (L. Alha).

0168-9002/$ - see front matter © 2008 Elsevier B.V. All rights reserved.
doi:10.1016/j.nima.2008.08.138

of instruments. The time resolution of 16 s enabled XSM to study rapid spectral variations during flares, e.g. changes in the coronal temperature and physical processes that contribute to the emission. The XSM data can also be combined with data obtained simultaneously by other solar observing instruments like GOES, SOHO, TRACE and RHESSI. Because of the large FoV (Field of View), XSM saw the Sun as a point source, hence the total X-ray irradiance of the Sun was recorded. These data are similar to the data obtained from astronomical X-ray satellites, e.g. XMM-Newton and Chandra observatories, which observe mainly objects outside the solar system. As also the spectral range and spectral resolution of XSM is close to those of XMM-Newton and Chandra, solar spectral data from XSM can be compared directly with the X-ray emission data of distant active stars and other point sources. An empirical modeling of stellar X-ray coronae can be made on the basis of observed spectra from XSM. This may shed new light on the question of differences and similarities between the solar corona and coronae of other stars.

1.3. *In-flight operation*

XSM had two basic observing modes, calibration mode and solar observing mode. The difference between these two modes was defined by the position of the shutter of XSM. In both modes the detector produced structurally similar data with the same integration time. While the acquisition was on, and the shutter was closed, XSM was calibrating. There was a ^{55}Fe calibration source attached in the inner surface of the shutter. The ^{55}Fe source was covered with a titanium foil about of 5 μm thickness. Hence, it emitted four distinct spectral lines: Mn Kα (5.8951 keV), Mn Kβ (6.4905 keV), Ti Kα (4.5088 keV) and Ti Kβ (4.9318 keV). Each nominal observation sequence began and ended with 20 calibration spectra. The integration time of one spectrum was 16 s. The data between the start and the end of calibrations are either solar or sky background spectra depending on the attitude of the SMART-1 S/C. The purpose of the calibrations before and after each observation was to get input information to characterize the detector response for any instance during the observations. The histogram in Fig. 1 illustrates the solar observation time of the XSM during the whole mission. The total solar integration time was nearly 439 h. The XSM sensor unit was located on the +X-panel of the spacecraft. The alignment of the optical axis with respect to the S/C frame of reference is described in Fig. 2.

The XSM sensor unit (Fig. 3) was an aluminum enclosure having a wall thickness of 3 mm. The unit contained a high purity silicon PIN (Positive Intrinsic Negative) diode detector, a Peltier cooler, front end electronics, and a shutter mechanism. The layout of the XSM PIN package is shown in Fig. 4. The detector crystal was a square chip with a side length of 5 mm and thickness of 0.5 mm. The active detector area was circular, with a diameter of 1.5 mm. There were three concentric guard rings surrounding the active detection area. The inactive dead layer of the front surface

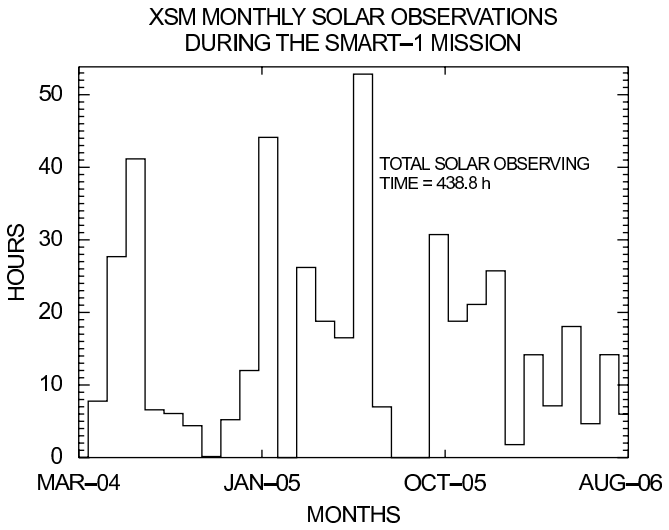

Fig. 1. Monthly solar observing time (hours) of the XSM during EEP and LP between 01.03.2004 and 31.08.2005.

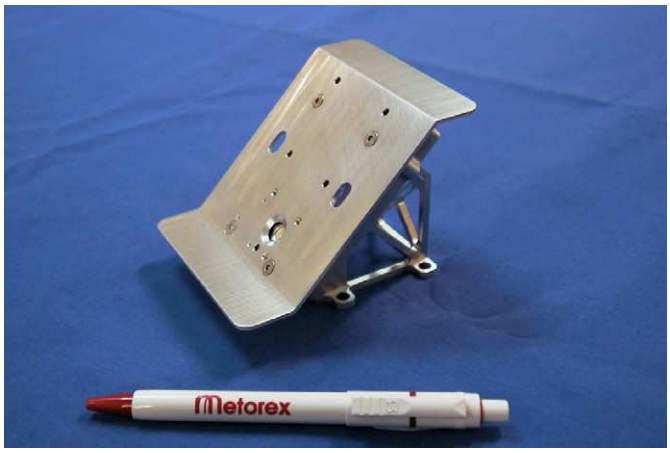

Fig. 3. XSM sensor box.

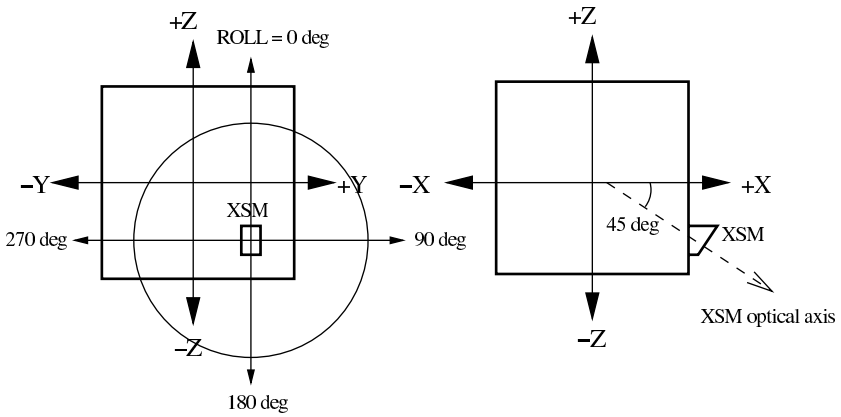

Fig. 2. The pointing of the optical axis of XSM detector in the SMART-1 S/C reference frame. The optical axis lies on the *XZ*-plane and it is directed 45° from the +*X*-axis toward the –*Z*-axis. The roll angle in the FoV is defined in the leftmost drawing. A roll of 0 corresponds to the +*Z*-axis direction and the roll increases clockwise.

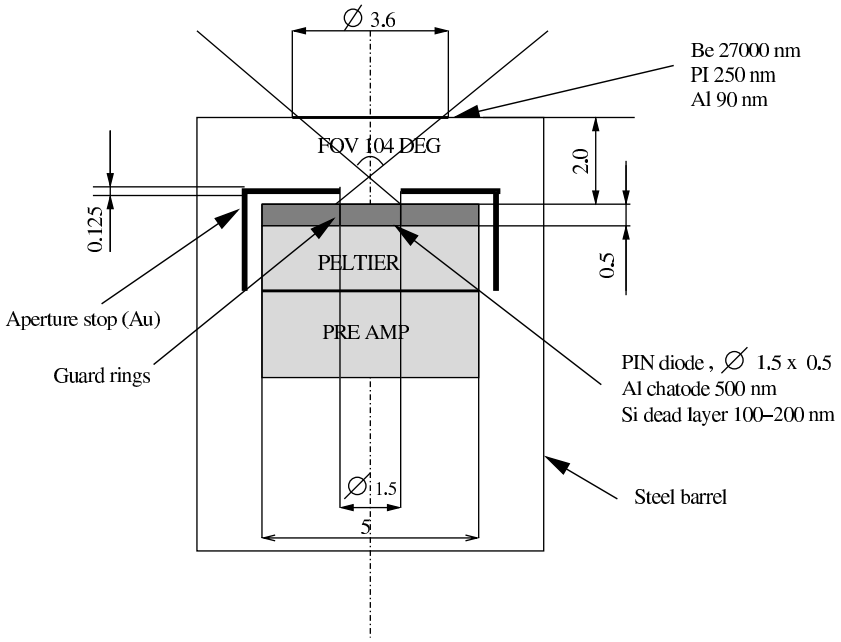

Fig. 4. Schematic layout of the XSM PIN enclosure and its dimensions.

Table 1
A collection of the XSM performance values

Nominal energy range	2.0–20.0 keV
Energy resolution (BOF)	250 eV at 5.9 keV
Number of channels	512
FOV (circular)	Diameter 104°
On-axis geometric area	0.0177 cm^2

of the detector diode was approximately 100 nm [6]. The front side of the PIN was coated with an aluminum layer of 500 nm acting as a cathode. The beryllium X-ray filter was 27μm thick. There was a compound filter layer made of 0.25μm PI (Polyimide), which was coated with an aluminum layer of thickness of 90 nm. The effective area of the detector was reduced by an aperture stop, a golden annular structure centered on the surface of the detector PIN. The primary task of this aperture stop was to inhibit the incomplete charge collection in the peripheral area of the silicon PIN. A second task of the aperture stop was to reduce the effective area of the PIN to obtain the required dynamical range in terms of count rate during extreme conditions, i.e. quiescent solar phase and at X-class flare events. A collection of the XSM performance values are shown in Table 1.

In the beginning of the mission the energy resolution was approximately 250 eV at 5.9 keV as determined with the ^{55}Fe calibration source. During the mission the energy resolution degraded by time mainly due to the high energy proton bombardment in space. It is commonly known that high energy particles cause lattice defects in the semiconductor materials, which increases the leakage current level, which in turn leas to a degraded energy resolution. The shutter mechanism was made of 0.7 mm tungsten to reduce the degrading influence of the space particle bombardment. The XSM control electronics was located in the D-CIXS detector unit, and the instrument front end (sensor unit) was connected with the electronic unit by an electrical cable of 2.7 m length. The control electronics was equipped with an autonomous logic to start auto annealing, when the leakage current level exceeded a pre-fixed trip level, which was a tunable parameter during mission operations. During annealing the Peltier current was reversed and it started to heat the PIN instead of cooling it. The temperature was increased up to 80° of Celsius for 5 h to anneal the PIN. The leakage current was monitored and its values were recorded in the House Keeping (HK) data. The recovery level of the leakage current was always slightly higher than the previous leakage current level, since the lattice defects were partly irreversible. The base tripping level of the leakage current was increased step by step during the mission. The base level was measured with the calibration source. The reset rate of the preamplifier was a function of the count rate, and the count rate of the calibration source was known. The initial activity of the ^{55}Fe source was known and the half life of this radioactive isotope is 2.73 years. This enabled the calculation of the expected count rate throughout the mission. The leakage current was a function of the count rate, hence the leakage current could be defined and read from the HK data. The use of the shutter slowed this degradation process. Due to the irreversible increase of the baseline leakage of the detector, the parameters controlling the autonomous annealing had to be changed frequently. The operational PIN temperature was adjusted between −5 and −20 °C. In the beginning of the mission the operational temperature was adjusted −20 °C. At the end of the EP (Extended Phase), it was increased close to −5 °C. One possible reason for this thermal change may be the degradation of the sensor box front surface material. The darkening of the Secondary Surface Mirror (SSM) material increases absorptivity. This could cause the whole sensor box to be heated up over 40 °C, when the Sun is in the FoV. The cooling power of the XSM Peltier was limited to a temperature difference of about 50 °C, and thus the lowest attainable detector temperature with the high sensor box temperature was about −5 °C, when the sensor box was exposed to the Sun.

2. Characterization of the instrument performance

The performance of an X-ray spectrometer has to be known very accurately to enable a reliable analysis of the obtained spectral data. In the case of XSM, the first step in the detector characterization process was the ground calibrations. Due to the

challenging and variable conditions in space, the characterization of the detector had to be repeated frequently as long as the mission went on. In practice this was realized by making in-flight calibrations in the beginning and at the end of each observation whenever possible.

2.1. Initial parameters from the ground calibrations

The XSM ground calibrations [7] were carried out at the X-ray laboratory, University of Helsinki in 2002. The XSM performance was tested in near vacuum conditions in a clean room environment. The main radiation source in the calibrations was a titanium X-ray tube. The most significant and surprising result found in the ground calibrations was the asymmetric FoV. Before the ground calibrations it was assumed that the sensitivity of the XSM FoV depends only on the off-axis angle, i.e. the angle measured from the optical axis to the target. Practically this would mean that the PIN was located exactly concentrically in the cylindrical detector steel enclosure, and the detector aperture should be perfectly circular. Based on this ideal assumption the shadow cast by the collimating edge of the steel enclosure should have been independent of the azimuthal direction, i.e. the roll angle. The FoV of the XSM was scanned with white light spectrum obtained from a titanium X-ray tube. XSM was attached on a turnable goniometer set and four diagonal scans across the FoV were made along the following roll angle directions: 0°/180°, 45°/235°, 90°/270° and 135°/315°. This test revealed an asymmetric response in the FoV, which was probably caused by either a slightly eccentric or tilted position of the detector PIN with respect to the collimating steel enclosure. The sensitivity of the off-axis angle was calculated beforehand assuming the system being symmetric. After finding the roll angle dependent behavior, the whole FoV sensitivity was modeled numerically using the scan results as input. To maximize the statistics of the measurements and respective accuracy of the analysis the energy range (7–9 keV) used to model this phenomenon was chosen so that the detector total quantum efficiency (QE) (including detector QE and transmission through filtering materials) was close to its maximum, i.e. 0.985 at 8.56 keV. The sensitivity of the FoV was tabulated in an array of size 401 × 401 (Fig. 5). Each array element represents a coordinate pair of off-axis and roll angles. The tabulated angular resolution was better than 1° in the array. The off-axis range was 0–52° and roll angles covered a full circle 0–360°.

The XSM observations were made without any specific pointing requirements set by XSM itself. Hence, the position of the Sun in the FoV of XSM was not known before it was determined from attitude history data. After the Sun position was determined from the S/C telemetry, the corresponding coordinate pair was chosen from the FoV table. This off-axis and roll angle pair was applied in the further analysis to generate final values for the effective areas.

2.2. Generation of the ancillary response file

An Ancillary Response File (ARF) is a FITS formatted file, which includes information of the effective area of the detector as function of photon energy. The effective area depends on the QE and the obscuration factor. Both of these are functions of the Sun's position in the FoV. The QE depends only on the off-axis angle, and the obscuration factor, i.e. the shadowing effect, depends on both angles. The angles corresponding to the Sun's position in the FoV were retrieved from the tabulated FoV array. The numerical content of this table is illustrated in Fig. 5 as a contour plot. To build an ARF for each solar spectrum, the position of the Sun must be known at each integration. The Sun's position relative to the instrument FoV was calculated using S/C attitude data as input. The QE curves were calculated according to the nominal filter and detector thicknesses given by the manufacturer of the detector.

A table containing 53 different effective area curves was calculated. Each curve represented one specific off-axis angle starting from 0° going up to 52° with interval of 1°. The total QE decreased with the off-axis angle. When the off-axis was greater than 50° at a roll angle of 180° or off-axis was greater than 47° at a roll angle of 0°, the Sun was out of the FoV and XSM started to measure the sky background. On the other hand, the QE or effective area increased at the high energy side due to the increasing thickness of the detector material, i.e. the stopping power of the silicon PIN increased. All the 53 distinct effective area curves are plotted in Fig. 6.

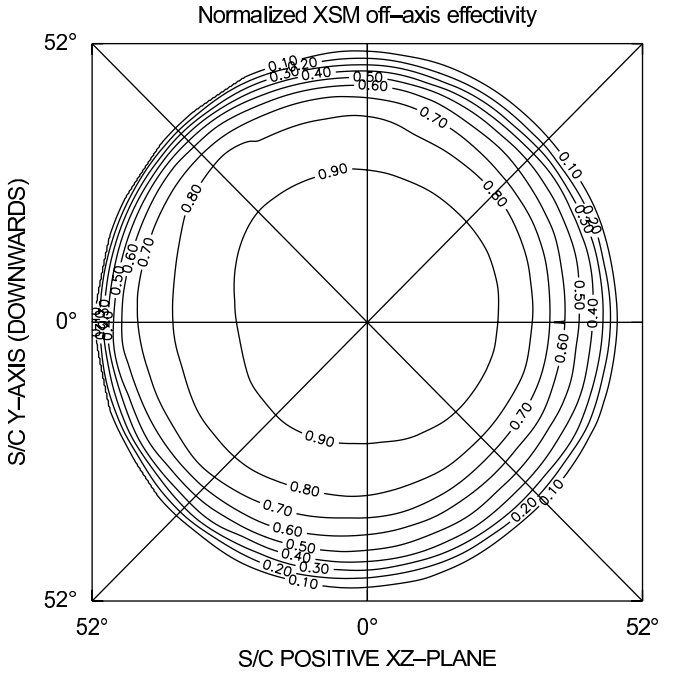

Fig. 5. XSM FoV sensitivity map, i.e. the obscuration factor derived from the off-axis and roll angles.

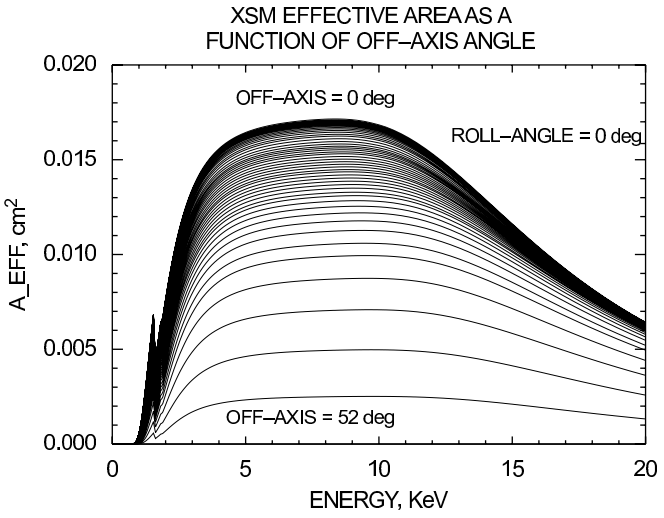

Fig. 6. Composition of 53 distinct effective area curves. Each curve represents a different off-axis angle calculated at 1° interval from 0° up to 52°.

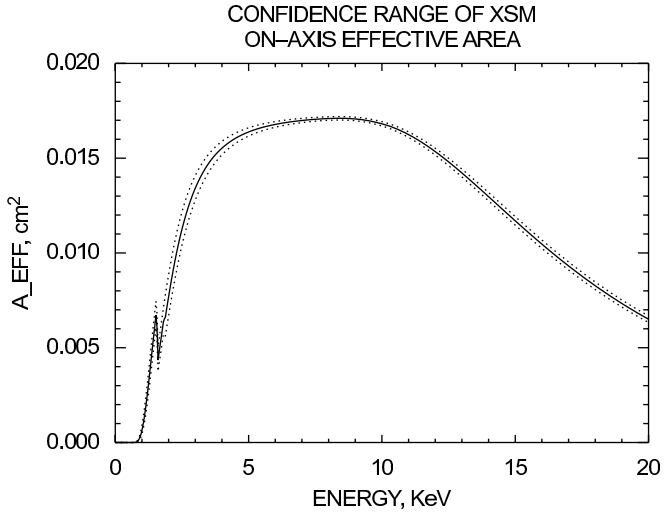

Fig. 7. Errors in XSM on-axis effective area. The dotted curves are derived from the extreme minimum and maximum values of filter and detector crystal thicknesses. The aperture stop diameter error is also included in above plots. The solid line in the center represents the XSM on-axis effective area calculated with nominal values.

Table 2
The minimum, nominal and maximum detector and filter dimensions of XSM

	value (μm)	value (μm)	value (μm)
Detector thickness, Si	485.0	500.0	515.0
Dead layer, Si	0.01	0.1	0.2
Cathode and filter, Al	0.53	0.59	0.65
PI-filter	0.22	0.25	0.27
Be-filter	24.5	27.0	29.5
Aperture stop diameter	1484	1488	1492

The tolerances are obtained from the manufacturer.

The error limits of the XSM effective areas are shown in Fig. 7. The two dotted curves represent the XSM on-axis effective area derived from the most extreme filter and geometrical values given by the manufacturer. The solid curve is the theoretically derived nominal on-axis effective area of XSM as a function of photon energy. The minimum and maximum values for each factor influencing on the XSM effective area are listed in Table 2.

2.3. Determination of the XSM effective area for full FoV

As for solar observations the sensitivity of XSM depended on the pointing determined by the S/C attitude relative to the Sun as explained above. In the nominal solar observations the Sun was regarded as a point source since its angular diameter is about 0.5° at 1 AU, which causes negligible deviation the results according to our estimates for present analysis. The roll ρ and off-axis θ coordinate pair angles within the circular FoV of 50° were used as a reference for the vignetting, i.e. the obscuration factor related to the shadowing caused by the collimating aperture structures. The QE was also dependent on θ, because the filter thicknesses were functions of $\sec\theta$. The generation of effective area for the solar observations was a straightforward task based on an obscuration factor table, which is a function of ρ and θ. This nominal method is not applicable for generating the ARF for the full FoV observations, e.g. for the X-ray sky background observations. In these observations the diffuse emission cameos from all over the

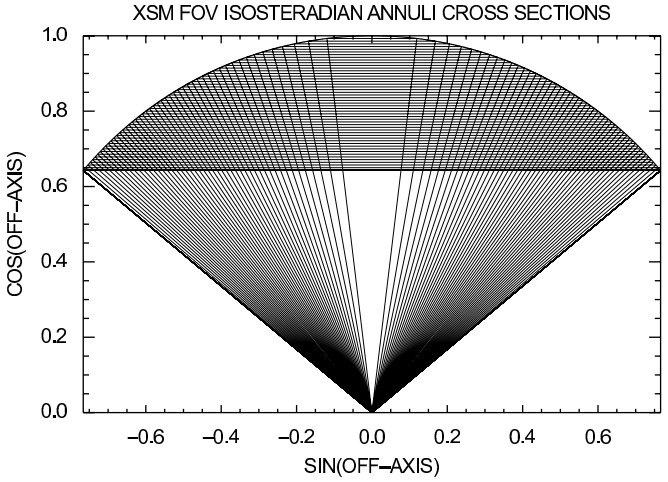

Fig. 8. The division of 50 equal FoV annuli.

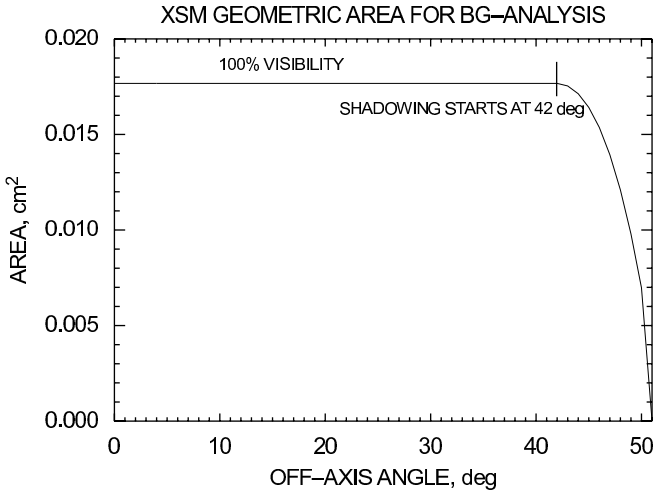

Fig. 9. The full FoV geometric area for background observations as a function of θ.

FoV into the detector including all the emission components of galactic and extragalactic point sources. Hence, we had to build a specially tailored effective area for the background observations, which is an averaged A_{eff} over the whole FoV with respect to effects related to the off-axis and roll angles. The first step was to divide the circular FoV into the 50 concentric annuli each having a solid angle of equal size. The formula for calculating the corresponding off-axis angles for the sky annuli is shown in Eq. (1). Fig. 8 illustrates the annular division in the FoV of XSM. The next step was to calculate the geometric detector areas and the respective QEs for the annuli for each fixed θ. The geometric full FoV curve is shown in Fig. 9. Each of the effective area was also multiplied with $\cos\theta$, because the intensity was decreased by this amount when a photon impinged the planar detector surface. Fig. 10 illustrates the plots of the deduced effective areas calculated at different values of θ. The final effective area for the background observations was the mean value of all these 50 distinct effective areas.

$$\theta_n = \arccos\left[1 - \frac{1-\cos(\theta_c)}{N}n\right], \quad \theta_c = 50^\circ, \quad n = 1,\ldots,N. \tag{1}$$

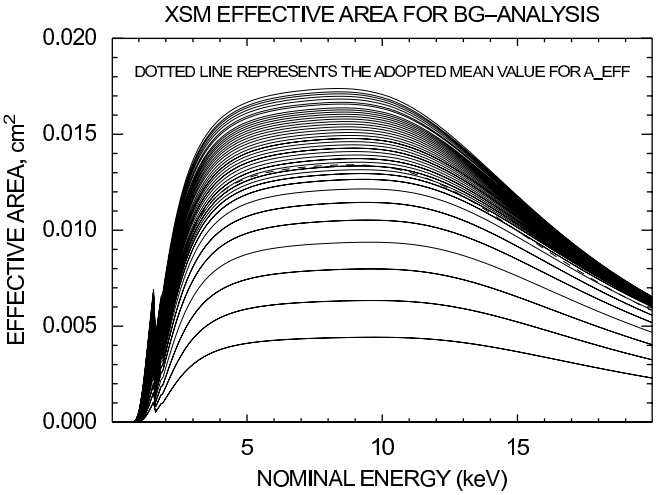

Fig. 10. The effective area curves of all the 50 annuli. The dotted and bold curve represents the effective area of the full FoV.

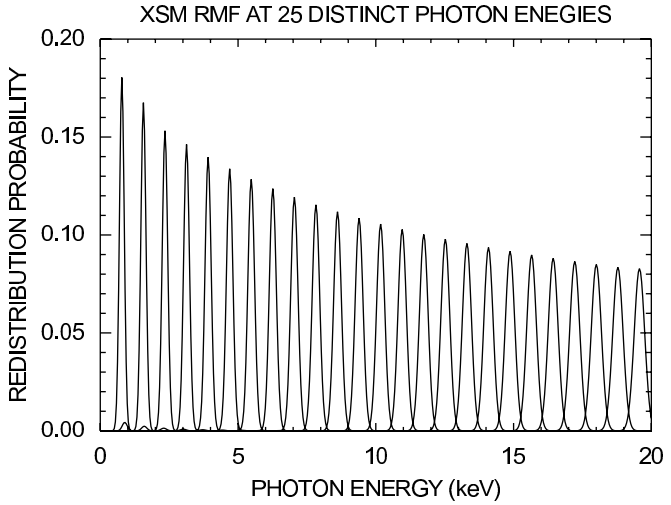

Fig. 11. XSM redistribution functions calculated at several different photon energies. The escape peak vanishes gradually as the energy increases.

2.4. Generation of redistribution matrix file

The spectral response of the detector is characterized by the Redistribution Matrix File (RMF). The essential part of the RMF is a redistribution function, which represents the probability of a single photon to be read into a certain energy channel. In the case of XSM, this function was composed of two discrete functions: a Gaussian main peak and an escape peak. Each column of the RMF array represented an energy bin and each row contained a specific redistribution function calculated at a fixed energy bin. The XSM electronics was configured with 512 energy channels. The nominal channel width was about 40 eV. The components of the redistribution function are shown in Eqs. (2) and (3). The main peak

$$G(E) = I_{h\nu} \exp\left[-\frac{(E-h\nu)^2}{2\sigma^2}\right] \quad (2)$$

is a Gaussian function of measured photon energy of $h\nu$ where h is the Planck constant and ν is the frequency. σ represents the total noise of the detector system and it determines the energy resolution of the detector. The escape peak

$$\mathrm{Esc}(E) = I_{\mathrm{esc}} \exp\left[-\frac{(h\nu-E-E_{\mathrm{esc}})^2}{2\sigma^2}\right] \quad (3)$$

is also a Gaussian function. Its peak centroid was just shifted 1.748 keV towards lower energies from the main peak. This shift is always constant and its value depends on the detector material. Because this redistribution function represents a probability, i.e. it had to be normalized to 1. Several redistribution curves are shown in Fig. 11.

The RMF contains also a second table, which includes the information of the energy boundaries, i.e. it determines the applied energy scale of the obtained spectral data. In the final spectral fittings, this energy scale was the reference scale for the applied RMF, ARFs and spectral data. This energy scale was defined by two parameters, which were the gain and the offset. The gain represents the energy width of each channel (eV/ch) and the offset represents the intersection point of the energy scale axis and the channel axis, i.e. the energy of the zeroth channel. The gain and the offset were deduced from in-flight calibration data. The centroids of the peaks, i.e. respective channel numbers of the Ti Kα and Mn Kα lines were calculated to find the relation between photon energy and channel number and the outcome of this computation was the two required parameters, i.e. gain and offset. The calculated energy scale was then inserted in the energy boundary array of the RMF. The energy resolution was also computed by using spectra of calibration data. A Gaussian function was applied to compute standard deviations for Ti Kα and Mn Kα lines. The energy resolution (FWHM) was determined throughout the energy scale from the resolutions at 4.5 keV and at 5.9 keV. Eq. (4) represents the relation between photon energy and energy resolution. By squaring both sides of this equation, one can define the parameters a and b with a linear fit:

$$\Delta E(E) = \sqrt{aE+b}. \quad (4)$$

3. In-flight performance

The XSM HK data include all essential operational information enabling a study of the performance of the detector during each observation. The most important HK values were the detector PIN temperature and the leakage current, because both have a direct influence on the energy resolution for this type of detectors. The count rate is a function of total leakage current and leakage current on the other hand depends strongly on temperature. The thermal conditions were always the most unfavorable, when XSM was observing the Sun, i.e. the sensor box was exposed to the Sun. The sensor box was heated up and more cooling power from the Peltier was required. The Peltier target temperature was the desired operational PIN temperature, which could be set by the on-board S/W. The detector sensor box temperature was also included in the HK data. If the box temperature was more than 50 °C higher than the desired operational PIN temperature, XSM could not dissipate out any more heat generated by the Peltier cooler. This situation lead to a thermal loop, and the detector never reached the desired operational target temperature. As a result, the thermal balance was not reached, since the Peltier was heated more than it cooled.

3.1. Thermal effects on energy resolution and energy scale

The energy resolutions of the Ti and Mn lines calculated at various times during the mission and the related HK values are shown in Table 3. The two parameters defining the energy scale, i.e. photon energy vs. channel number relation, are also listed. This linear relation was determined by the gain (eV/channel) and the offset. Describing the time evolution of the XSM performance, it should be notice that the energy resolution was fairly stable. The

Table 3
The time evolution of the XSM performance studied with the following parameters: Energy resolutions at 4.5 and 5.9 keV, gain, offset, PIN temperature and leakage current

2004.03.03T01:13:40	252	296	42.8	−242	−14.7	7.0
2004.04.26T02:34:38	267	310	43.2	−324	−9.4	8.6
2004.05.24T06:47:47	279	323	43.4	−378	−9.3	11.3
2004.06.25T23:30:03	303	326	42.9	−359	−8.4	10.2
2004.07.23T04:09:23	309	320	43.0	−339	−9.4	9.6
2004.08.17T22:18:35	264	330	43.0	−397	−9.4	9.0
2004.09.06T19:36:04	311	328	43.1	−366	−7.7	10.7
2004.10.18T21:35:01	315	320	44.7	−410	−9.2	7.4
2004.11.03T01:16:19	287	323	43.4	−357	−9.4	10.3
2005.01.15:04:51:56	290	321	42.9	−335	−9.3	9.1
2005.05.19T01:26:01	330	333	43.3	−374	−9.4	9.3
2005.07.03T06:33:24	304	332	42.6	−327	−9.4	8.7

All the values at the same row are derived from the same calibration data.

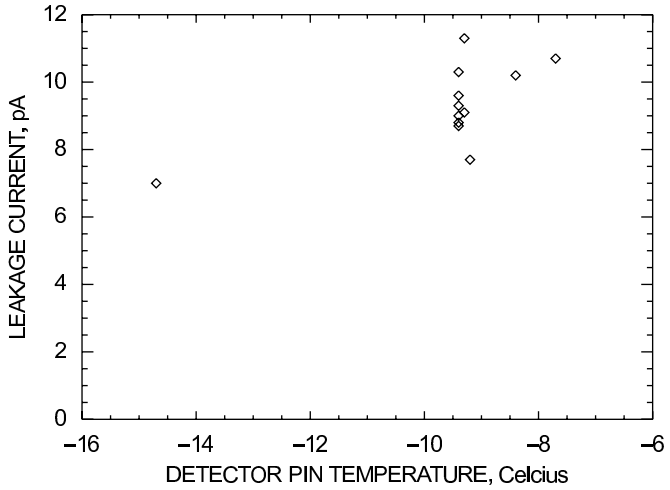

Fig. 12. The relation between the operational PIN temperature and detector leakage current.

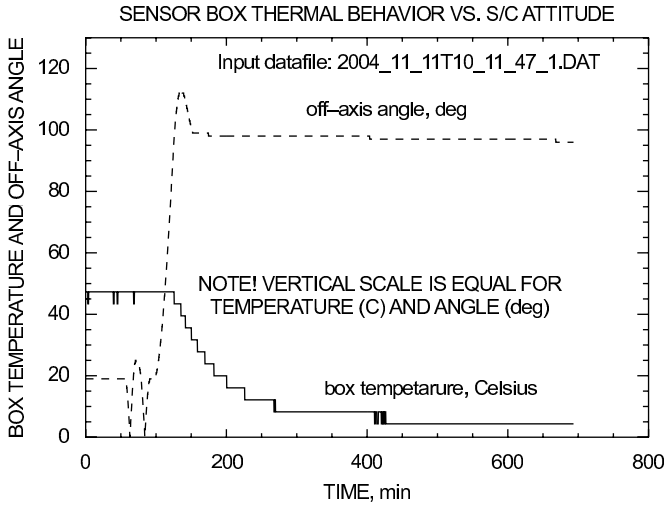

Fig. 13. The box temperature during S/C attitude change. The heating of solar radiation stops, when the off-axis angle comes greater than 90 °, i.e. XSM is in the shadow. This plot is generated from the same data file as is used to define the gain shift shown in (Fig. 14).

total increase in the FWHM was roughly 36 eV at 5.9 keV during the whole mission. The best energy resolution was obtained in the first sample of calibration data. This can be explained by the smaller particle dose level in the early phase of the mission, i.e. the lattice defects were insignificant. In this first calibration the average PIN operational temperature was −14.7 °C, which was the lowest value among the data samples. The resolutions calculated for the Ti Kα-lines at 4.51 keV varied oddly. This was probably related to the fitting routine applied and the blending of the Ti Kα-line (4.51 keV) with the Ti Kβ-line (4.93 keV).

Looking at the plot in Fig. 12 obtained from the two last columns (see Table 3), one can see the correlation between the operational the temperature and the leakage current. It is known that the sensor box temperature had an influence on the gain. The variation with respect to the detector gain was related to the pre-amplifier, whose operation was affected by the ambient temperature [8]. This gain change was studied with the data obtained on the 11th of November in 2004. These data included a long run of 8609 calibration spectra, equaling an integration time of more than 38 h. During this integration the S/C attitude changed so that the XSM off-axis angle varied between 0° and 120° as seen in Fig. 13.

The test-RMF was generated by applying 20 calibration spectra in the beginning and at the end of the integration. The gain, offset, and line resolutions were calculated from the mean values of those calibration spectra. Eleven different sub data files were made of intermediate calibration spectra obtained from this specific long run. Each file consisted of a sum of 10 calibration spectra taken at different box temperatures. All files containing calibration line spectrum were fitted by applying the generated nominal test-RMF. The fitted positions of Mn Kα-lines as a function of the box temperature are shown in Fig. 14. The fitted line energies were close to the correct value at the box temperature range between 10 and 15 °C. The horizontal constant line crossing the plot represents the theoretical value for the Mn Kα-line energy 5.8951 keV. One should take this phenomenon always account, when doing spectral fittings. Models containing Gaussian line components require special tuning related to the generation of the energy scale. A nominal way to generate the RMF is not sufficient for fitting Gaussian lines accurately. One should use a specially tailored energy scale for individual spectra, i.e. a separate RMF must be generated for each fitted spectrum, if the box temperature has varied significantly during a long integration.

3.2. Instrument background

The instrument background of the XSM was expected to be very low due to the small detector area of 0.0177 cm^2. This low

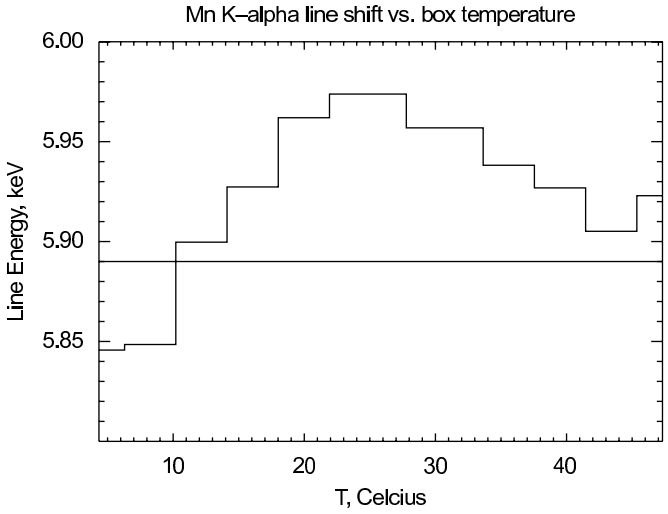

Fig. 14. The deviation of Mn Kα-line as a function of sensor box temperature.

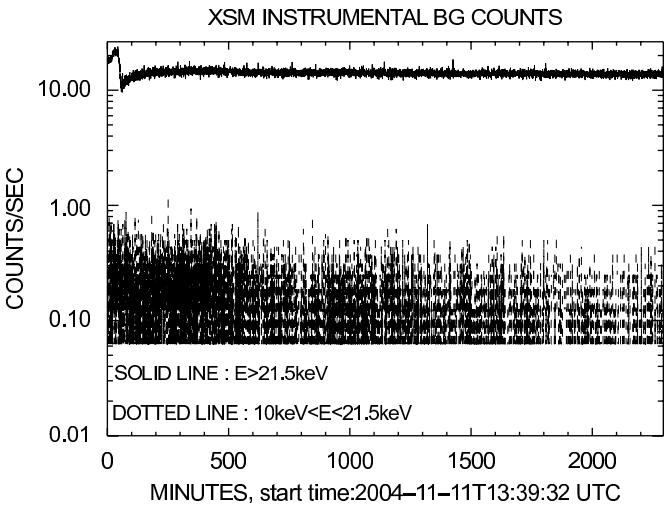

Fig. 15. XSM instrumental background count rate at two energy bands with the shutter closed.

level instrument background was verified by analyzing the count rates of the calibration spectra at two different energy bands. The analyzed data were a long integration with the shutter in closed position. The instrument count rate at the lower energy band between 10 and 21.5 keV was less than 1.0 ct/s (see Section 6.6). The count rate in the last channel was slightly higher, because it contained all the events having energy above 21.5 keV. The calibration source counts all lied below 7 keV and did not contribute to the analyzed energy bands. The count rate between 10 and 21.5 keV was so low that there was no need to take them into account in the final spectral analysis. The instrument background was greater than the value given here, because the observations were done with the shutter in open position. This enabled particles to impinge freely into the detector through the solid angle of 2.24 sr. Fig. 15 illustrates the count rates at two different energy bands obtained from this long calibration integration.

3.3. Count rate anomaly

By analyzing the calibration spectra of the XSM obtained along with the solar observations throughout the mission, we found excess counts in a number of spectra. The extra counts occurred always simultaneously with noise in the low and/or high energy channels of the spectra, which was not related with X-ray signal emitted by the calibration source. We derived a preliminary correction function to the calibration spectra based on the difference in the expected and observed counts from the calibration source, and the total counts in the energy channels 0–20. The reason for this anomaly may be related with the loss-free counting system [9] applied in the XSM readout electronics. The observed anomaly has serious consequences to the analysis of solar X-ray spectra observed by the XSM, and a detailed quantitative analysis of the excess counts is needed to obtain reliable scientific results from spectra disturbed by this phenomenon. Spectra including these excess counts are currently not used for quantitative scientific analysis of solar X-ray emission. A paper on the analysis of the excess counts and their effects on the solar spectra is being prepared and it will be published in near future.

3.4. FoV asymmetry

The FoV of XSM was analyzed during the ground calibration tests with an X-ray tube. A white beam was collimated to make the beam represent a source at infinity. In practice the test beam was slightly broadened. The scan across the direction from roll angle of 0° to roll angle of 180° revealed a slight asymmetry in azimuthal direction. In the laboratory measurements, the limiting off-axis angle at roll angle of 180° was close to the nominal 52° and the respective limiting off-axis angle at roll angle of 0° was about 49°. By investigating the XSM flight data we found that the XSM limiting off-axis angle at roll-angle of 0° was about 47° instead of 49°. This limiting angle was best seen in the data obtained on the 3rd of June 2004, while the S/C attitude changed rapidly during the XSM observation. At that time the off-axis angle decreased almost linearly from 54° down to 0° in 464 s. The count rates corresponding to the solar X-ray output between channels 20 and 150 of the spectra were studied to find out the off-axis angle representing the zero level count rate. This count rate drop occurred right after the spectrum obtained at the off-axis angle of 47°. The solar activity according to the GOES data at that time interval was steady and about 10^{-7} W/cm^2 at 1.55–12.4 keV range. Hence, the solar intrinsic X-ray activity had no influence on the change of count rate in this analysis. The nominal XSM FoV off-axis range was calculated by using the ideal

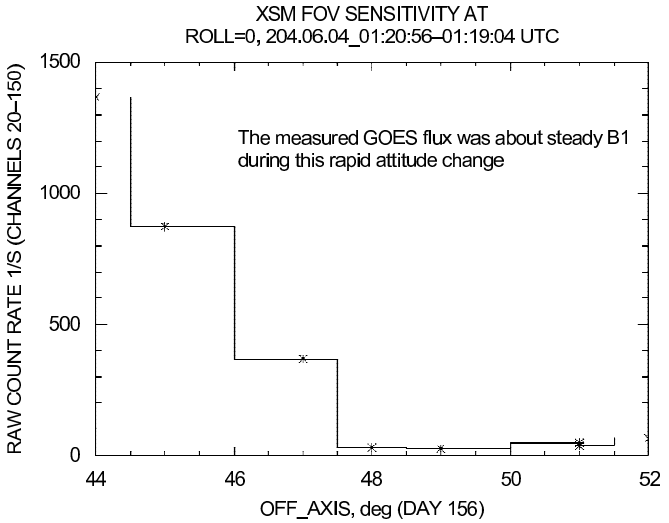

Fig. 16. The raw count rate vs. off-axis angle. (The time domain is reversed related to the real observation!)

geometrical dimensions given by the manufacturer. In practice the limiting off-axis was approximately 47° at roll angle equal to 0° instead of 49° obtained from ground calibrations. We do not have a clear explanation for this discrepancy asymmetry in azimuthal direction. We can rule out the malfunction of the shutter, because no counts from the calibration source were seen in the spectra when the off-axis was close to 47° at a roll angle of 0°. Possible reasons for the 2° difference are discussed in Section 2.1. The derivation of the limiting off-axis angle at roll equal to 0° is shown in Fig. 16. It should be noted, however, that this discrepancy does not imply significant errors in analysis performed earlier, since the detector efficiency is very small at all off-axis angles greater than 45°.

4. Data analysis

The raw telemetry data were first converted and sorted into several different FITS files each representing a specific data type. The next step was to generate a FITS table, which applied HK and spectral data as inputs with the corresponding attitude data. This table included all essential HK values and attitude information, e.g. off-axis and roll angles related to each spectrum. The table also included effective areas for each spectrum. This data table was the final archived data product. It contained all data needed to make the final analysis, e.g. the generation of ARFs, RMSs and spectral FITS formatted data suitable as inputs for the XSPEC [10] S/W. It is worth to mention that all XSM related FITS formatted data products can be read and visualized with the ftools [11] S/W. This public science S/W package also includes the XSPEC spectral fitting program.

4.1. Solar flare observation by XSM

The first solar flare observation with XSM was obtained on the 24th May, 2004 at 11:05:00 UTC. The solar spectrum between 5.0 and 9.0 keV of this C4-class flare is shown in Fig. 17. The spectral fittings made with XSPEC revealed several phenomena, the most interesting being the iron lines at about 6.65 and 7.92 keV. These highly ionized iron lines correspond to a coronal temperature of greater than 10 MK. This iron line emission was only visible during flares. It declined rapidly after the flare has peaked. The spectral model was composed of a bremsstrahlung and two Gaussian lines.

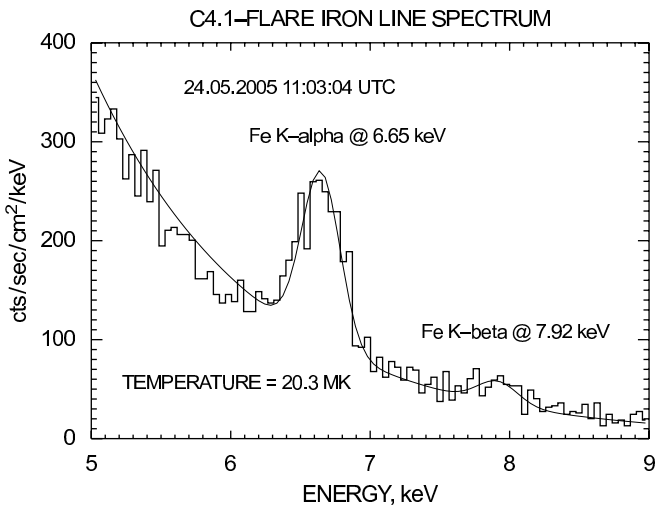

Fig. 17. The distinct initial Fe-lines at 6.64 and 7.83 keV. These emission lines correspond to highly ionized iron, i.e. helium like Fe XXIV or hydrogen like Fe XXV Kα and Kβ lines.

The fitted line energies corresponded to highly ionized hydrogen like Fe XXIV. The model flux for the respective lines was 4589 (at 6.65 keV) and 626 photons/cm^2 s (at 7.92 keV). This yielded a flux ratio of 0.14, which is close to the theoretical value of about 0.11 representing the Fe Kα-and Fe Kβ-line flux ratio [12]. All the XSPEC fitting parameters and respective errors are listed in Table 4. The last columns include the derived fluxes of the fitted lines.

The iron Kα line energy of 6.65 keV corresponded to at least an ionization stage of Fe XXIII or even Fe XXIV [12]. The iron Kβ line of 7.92 keV was vary weak in the data and its energy determination suffered from inaccuracy in the fitting. The line energy of 7.92 keV corresponded to ionization stage of Fe XXVI, which mismatches with the iron Kα line energy of 6.65 keV. The bremsstrahlung model component kT of 1.65 corresponds to a flare temperature of 20.3 MK.

There are two light curves in Fig. 18, describing the time evolution of the flare intensity. The upper graph represents the total counts of the flare and the lower graph represents the Fe Kα-line counts obtained from the energy interval between 6 and 7 keV. This plot was made of using raw data, i.e. the fluxes are not derived from XSPEC. The purpose of this plot is to show the characteristic time evolution of the Fe-line.

4.2. Flux cross-calibration with GOES

The XSM solar data were also cross-calibrated with GOES (Geostationary Operational Environmental Satellite) solar X-ray data [13]. The first results show that the deduced flux levels

Table 4
The iron line energies fitted with XSPEC

Model component	Unit	Value	Error	Line flux (photons/cm^2/s)
Bremss (kT)	Unit less	1.650	±0.008	–
Gaussian (LineE)	keV	6.650	±0.008	4589
Gaussian (LineE)	keV	7.921	±0.032	626

Model components and their values are listed with errors. The calculated line fluxes of both iron lines are included in the last column.

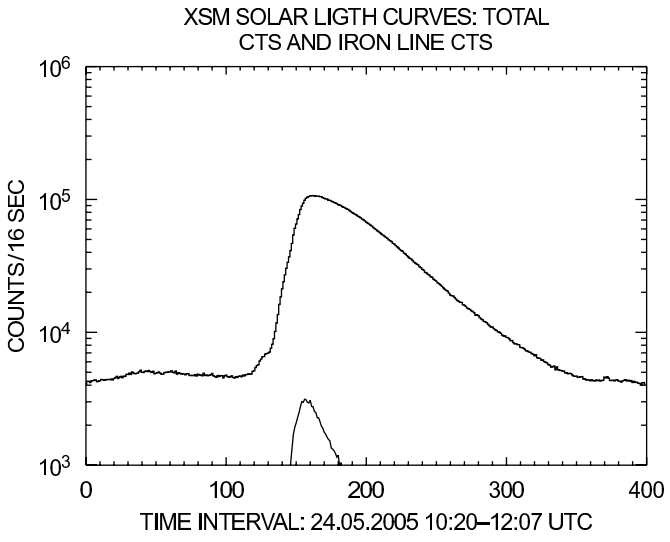

Fig. 18. The lower graph illustrates the evolution of the emission of Fe-line intensity along the peaking flare. The Fe-line disappears soon after the flare has peaked.

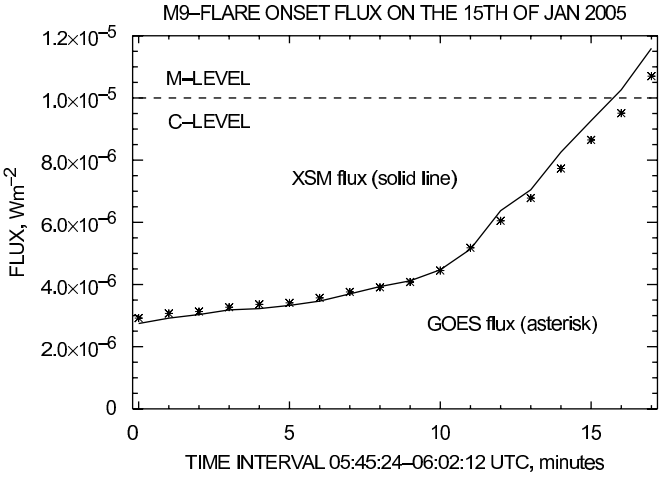

Fig. 19. Simultaneous XSM and GOES X-ray fluxes during a flare onset. The solid line represents XSM data and the crosses represent respective GOES data points.

obtained from the GOES and XSM were consistent. GOES and XSM fluxes obtained on 15th of January 2005 are shown in Fig. 19.

In these data the flux level rose up to M1-level, when the observation was interrupted. This was the highest flux level XSM ever observed. The best model to fit flare data within XSPEC was the broken power law model added with several Gaussian lines. The applicability of broken power law model was an obvious indication that the spectral model related to the XSM solar M1-flare X-ray data should include an emission model of at least two temperature components. Bremsstrahlung model with Gaussian lines was also applicable, e.g. when fitting quiescent solar spectral data and flares up to C-level. When fitting quiescent solar spectra, the fits must include also a background emission component together with a bremsstrahlung model. The background model is derived from the XSM off Sun observations. The XSPEC power law and cut-off power law models were well suited for the modeling of diffuse X-ray sky background.

5. Conclusions

XSM on-board the SMART-1 produced over 600 h of solar and background observations in total. Flares up to level M1 were observed. The best observations were made during the EEP (Earth Escape Phase), when there were long steady pointings. One of these was the first detection of the iron line emission on the 24th of May 2004.

The sky background observations enabled the generation of a rough map of the diffuse X-ray sky. (The results of this analysis will be published in 2008.) The flux cross-calibrations with the GOES showed that XSM measured solar X-ray fluxes at the same energy range with the accuracy of 10% compared to the simultaneous GOES observations.

There is still plenty of analysis to do with the XSM data, e.g. fitting all the observed flares from the onset down to the declining phase in order to determine the evolution of temperature and emission measure with in time. There are also interesting emission lines seen in the solar flare spectral data, which will be studied spectroscopically in the near future.

There were some drawbacks compared to the expected operation of XSM, e.g. the thermal problems, phantom counts and the unused energy range between 1 and 2 keV. The nominal energy range of the XSM was designed to start at 1 keV. Due to a misunderstanding, the real measured energy range was limited significantly above 1 keV. In practice the low energy limit was about 1.8 keV along the whole mission. This was the worst drawback related to the in-flight operation of the XSM. However, we were able to extrapolate the spectrum in the energy interval between 1 and 2 keV with the aid of spectral fitting done above 1.8 keV.

Acknowledgments

The Academy of Finland is acknowledged for financial support for this work, including Grants 205790, 74882, and 211061 for SMART-1 science for 2001–2005. Agency for Technology and Innovation TEKES is acknowledged for financing of the development of the XSM instrument.

References

[1] G.D. Racca, A. Marini, L. Stagnaro, J. van Dooren, et al., Planet. Space Sci. 50 (2002) 1323.
[2] B.H. Foing, G.D. Racca, A. Marini, D.J. Heather, D. Koschny, M. Grande, J. Huovelin, et al., Adv. Space Res. 31 (2003) 2323.
[3] B.H. Foing, G.D. Racca, A. Marini, E. Evrard, et al., Adv. Space Res. 37 (2006) 6.
[4] M. Grande, J. Huovelin, P. Muhli, P.J. Hakala, et al., Planet. Space Sci. 51 (2003) 427.
[5] J. Huovelin, L. Alha, H. Andersson, T. Andersson, et al., Planet. Space Sci. 50 (2002) 1345.
[6] H. Andersson, Personal communication with the representative of manufacturer, Oxford Instruments Analytical, former Metorex Inc., Finland.
[7] J.K. Laukkanen, et al., Calibration Report, S1-CIX-TR-3919, XSM Sensor Unit On-Ground Calibration, University of Helsinki, 2002.
[8] H. Andersson, Personal communication with the representative of manufacturer, Oxford Instruments Analytical, former Metorex Inc., Finland.
[9] G.P. Westphal, Nucl. Instr. and Meth. 163 (1979) 189.
[10] K.A. Arnaud, in: G. Jacoby, J. Barnes (Eds.), Astronomical Data Analysis Software and Systems V, ASP Conf. Ser., vol. 101, 1996, p. 17.
[11] J.K. Blackburn, in: R.A. Shaw, H.E. Payne, J.J.E. Hayes (Eds.), Astronomical Data Analysis Software and Systems IV, ASP Conf. Ser., vol. 77, ASP, San Francisco, 1995, p. 367.
[12] F. Nagase, PASJ 41 (1989) 1 (Fig. 17 in Nagase 1989).
[13] M.K. Väänänen, Cross calibration of XSM with GOES and RHESSI, Solar Physics (2009), to be published.